MNRAS **000**, 1–10 (2015) Preprint 9 April 2018 Compiled using MNRAS LATEX style file v3.0

3D radiative transfer of intrinsically polarized dust emission based on aligned aspherical grains

G. H.-M. Bertrang,[1,2,3,4]★ S. Wolf[1]
[1] *Kiel University, Institute of Theoretical Physics and Astrophysics, Leibnizstr. 15, 24118 Kiel, Germany*
[2] *Universidad de Chile, Departamento de Astronomía, Casilla 36-D, Santiago, Chile*
[3] *Universidad Diego Portales, Facultad de Ingeniería, Av. Ejército 441, Santiago, Chile*
[4] *Millennium Nucleus Protoplanetary Disks in ALMA Early Science, Universidad de Chile, Casilla 36-D, Santiago, Chile*

Accepted 2017 May 1. Received 2017 April 28; in original form 2016 June 7

ABSTRACT
(Sub-)Millimeter observations of the polarized emission of aligned aspherical dust grains enable us to study the magnetic fields within protoplanetary disk. However, the interpretation of these observations is complex. One must consider the various effects that alter the measured polarized signal, such as the shape of dust grains, the efficiency of grain alignment, the magnetic field properties, and the projection of the signal along the line of sight. We aim at analyzing observations of the polarized dust emission by disentangling the effects on the polarization signal in the context of 3D radiative transfer simulations. For this purpose, we developed a code capable of simulating dust grain alignment of aspherical grains and intrinsical polarization of thermal dust emission. We find that the influence of thermal polarization and dust grain alignment on the polarized emission displayed as spatially resolved polarization map or as spectral energy distribution trace disk properties which are not traced in total (unpolarized) emission such as the magnetic field topology. The radiative transfer simulations presented in this work enable the 3D analysis of intrinsically polarized dust emission – observed with, e.g., ALMA – which is essential to constrain magnetic field properties.

Key words: protoplanetary discs – radiative transfer – polarization – radiation mechanism: thermal – magnetic fields

1 INTRODUCTION

Various physical processes in protoplanetary disks are affected by magnetic fields. Magnetic fields influence the transport of dust and gas (e.g., Ciesla 2007; Turner et al. 2014), the disk chemistry (e.g., Semenov & Wiebe 2011), and the migration of planetesimals within the disk (e.g., Dzyurkevich et al. 2010). Even more importantly, magnetohydrodynamic (MHD) turbulence can provide the source of viscosity that expedites the accretion (Lynden-Bell & Pringle 1974), and thus, the evolution of the disk (Shakura & Sunyaev 1973). One of the most promising mechanisms for driving turbulence, respectively accretion is the magneto-rotational instability (MRI; Balbus & Hawley 1991, 1998). Turbulence in unmagnetized disks is unable to redistribute angular momentum in the disk sufficiently effective, thus, magnetic fields are needed to enable Shakura-Sunyaev viscosity (Balbus et al. 1996). The ionization fraction in the disk is high enough for magnetic coupling of material over large parts of the disk especially the thermally ionized inner disk and the highly ionized outer disk parts (e.g., Turner et al. 2007; Cleeves et al. 2015; Flock et al. 2015). Yet, constraining the magnetic field properties of the disk observationally, its strength and structure, is still at the beginning. First observations of very young, embedded protoplanetary disks performed with SMA, CARMA, and VLA show polarized signals which can be interpreted as indications for toroidal magnetic field structures (Rao et al. 2014; Stephens et al. 2014; Segura-Cox et al. 2015). Despite of non-detections found in more evolved protoplanetary disks performed with the SMA (Hughes et al. 2009, 2013), recent ALMA observations revealed the polarization strength and structure of the protoplanetary disk HD142527 on a hitherto unreached spatial resolution (Kataoka et al. 2016).

Spatially resolved observations of polarized millimeter continuum emission of aligned dust grains are best suited to reveal the magnetic field strength and structure in the protoplanetary disk (e.g., Weintraub et al. 2000; Cho & Lazarian 2007). However, the polarization signal is strongly influenced by many factors, e.g., dust grain shape, dust grain

★ E-mail: bertrang@das.uchile.cl

alignment efficiency, magnetic field properties, the spatial resolution of the observation, the projection along the line of sight, and the influence of self-scattered thermal emission (Kataoka et al. 2015, 2016; Yang et al. 2016). To take these effects into account, radiative transfer simulations are needed as analysis tools for intensive interpretation and prediction of observational results. A first approach has been undertaken by Cho & Lazarian (2007), henceforth CL 07. CL 07 employ a two-layered model of a flared circumstellar disk based on Chiang et al. (2001). In this model, the surface layer contains small dust grains, while the interior of the disk is filled with large grains. Each layer has its own, constant temperature, possible photon paths are limited, and the radiation field has been fixed to perfect anisotropy. Based on this simplified model, CL 07 predict that multi-wavelength infrared polarimetric studies of circumstellar disks can provide details on their magnetic field structure. Motivated by their findings, we aim at a more sophisticated treatment of aligned aspherical dust grains in protoplanetary disks and their intrinsically polarized thermal emission. We present here a 3D radiative transfer study considering the effects of polarized dust emission and dust grain alignment of aspherical grains that has been performed with an extended version of the established radiative transfer code MC3D (Wolf et al. 1999; Wolf 2003).

This paper is organized as follows. The alignment of aspherical grains and implemented approach of polarized thermal dust emission are introduced in Sect. 2 and Sect. 3. The simulation software is introduced in Sect. 4. Applications of this study are shown in Sect. 5. A final discussion and conclusions are given in Sect. 6.

2 ALIGNMENT OF ASPHERICAL GRAINS

Within protoplanetary disks, dust grains are assumed to be aligned along the magnetic field by radiative torques (e.g., Lazarian et al. 2015). In the presence of an anisotropic radiation field, aspherical dust grains, which have different cross sections for left- and right-handed polarized light, get aligned with their longest grain axis perpendicular to the magnetic field (Dolginov & Mytrophanov 1976; Lazarian 2007). Additional grain alignment mechanisms, i.e., paramagnetic alignment and mechanical alignment by either supersonic or subsonic flows, are negligible in protoplanetary disks: Paramagnetic alignment (Davis & Greenstein 1951) affects only dust grains smaller than 0.1 μm (Lazarian et al. 2015; Andersson et al. 2015). Mechanical alignment by supersonic flows (Purcell 1969) does not occur because of purely widely observed subsonic velocities, (e.g., Hughes et al. 2011) and because of the subsonic nature of MRI turbulence (Flock et al. 2011). And mechanical alignment by subsonic flows (Lazarian & Hoang 2007) appears to be inefficient in general, since aspherical grains may not show well-defined helicity in the process of grain interaction with gaseous flows (Lazarian et al. 2015; Andersson et al. 2015). In brief, the usual picture of aspherical grains aligned perpendicular to magnetic field lines applies. The polarized thermal emission of these grains traces the magnetic field within a protoplanetary disk.

We implement radiative torques in the 3D radiative transfer code MC3D on the basis of the approach outlined by CL 07. This approach allows us to consider the effect of radiative torques in a sophisticated disk model, taking the anisotropy of the radiation field into account. The mathematical description of radiative torques used in this implementation as well as in CL 07 goes back to the fundamental work of Draine & Weingartner (1996).

Dust grains in a protoplanetary disk are exposed to a radiation field, consisting of the emission of the central star and the emission of the dust itself. Thus, the grain is subject to a steady radiative torque. For the alignment of a grain, it is necessary that its rotational energy exceeds pure thermal motion. This ratio is commonly expressed by the factor (Draine & Weingartner 1996):

$$\left(\frac{\omega_{\mathrm{rad}}}{\omega_{\mathrm{T}}}\right)^2 = \frac{5\alpha_1}{192\delta^2}\left(\frac{u_{\mathrm{rad}}}{n_{\mathrm{H}}k_{\mathrm{B}}T}\right)^2\left(\frac{\rho a_{\mathrm{eff}}\lambda^2}{m_{\mathrm{H}}}\right)\cdot \cdot \gamma_{\mathrm{rad}}^2\,\langle \mathbf{Q}_\Gamma(\theta,\varphi)\rangle^2\cdot \mathbf{a}_1^2\left(\frac{\tau_{\mathrm{drag}}}{\tau_{\mathrm{drag,gas}}}\right)^2 \tag{1}$$

$$= 4.72\times 10^9\cdot \frac{\alpha_1}{\delta^2}\rho_3 a_{-5}\cdot \cdot \left(\frac{\gamma_{\mathrm{rad}}\cdot u_{\mathrm{rad}}}{n_{\mathrm{H}}k_{\mathrm{B}}T}\right)^2\left(\frac{\lambda}{1\,\mu\mathrm{m}}\right)^2 Q_\Gamma^2\left(\frac{\tau_{\mathrm{drag}}}{\tau_{\mathrm{drag,sgas}}}\right)^2, \tag{2}$$

where ω_{rad} is the angular frequency due to radiative torques, ω_{T} the thermal angular frequency, which is the rate at which the rotational kinetic energy of the grain is equal to $k_{\mathrm{B}}T/2$, $Q_\Gamma = \langle \mathbf{Q}_\Gamma(\theta,\varphi)\rangle\cdot\mathbf{a}_1$ is the efficiency factor of radiative torques, the geometrical parameters $\delta \approx 2$, $\alpha_1 \approx 1.745$ for a grain with axis ratio 2:2:1, gas mass density $\rho_3 = \rho/3\,\mathrm{g\,cm^{-3}}$ (assuming a gas-to-dust ratio of 100), and $a_{-5} = a/10^{-5}\mathrm{cm}$ is the equivolume grain radius. The degree of anisotropy γ_{rad} is defined by

$$\gamma_{\mathrm{rad}} = \frac{\left|\int_\Omega I_\lambda(\mathbf{k})\,\mathbf{k}\,\mathrm{d}\Omega\right|}{\int_\Omega I_\lambda(\mathbf{k})\,\mathrm{d}\Omega}, \tag{3}$$

with the wave vector $\mathbf{k}$, the wavelength-dependent intensity I_λ, and the solid angle Ω (Bethell et al. 2007). The degree of anisotropy lies in the range of [0, 1], where 0 corresponds to an isotropic radiation field and 1 to an unidirectional radiation field. The here presented temperature and anisotropy simulations are conducted self-consistently over a wavelength spectrum from 0.5 μm to 1000 μm.
The rotational damping time (Draine & Weingartner 1996),

$$\tau_{\mathrm{drag}}^{-1} = \tau_{\mathrm{drag,gas}}^{-1} + \tau_{\mathrm{drag,em}}^{-1}, \tag{4}$$

is composed of (i) rotational damping caused by gas-dust collisions,

$$\tau_{\mathrm{drag,gas}} = \frac{\pi\alpha_1\rho a_{\mathrm{eff}}}{3\delta n_{\mathrm{H}}\,(2\pi m_{\mathrm{H}}k_{\mathrm{B}}T)^{1/2}}, \tag{5}$$

and of (ii) rotational damping caused by absorption and emission of photons by the grain (Purcell & Spitzer 1971; Roberge et al. 1993). Assuming that the grain is heated by the star to a temperature T_{dust}, the damping time due to thermal emission may be written as

$$\tau_{\mathrm{drag,em}} = \frac{8\,\alpha_1\,(\beta+3)}{5}\,\frac{\zeta(\beta+4)}{\zeta(\beta+3)}\,\frac{\rho a_{\mathrm{eff}}^3\,(k_{\mathrm{B}}T_{\mathrm{dust}})^2}{\hbar c u_{\mathrm{rad}}\,\langle Q_{\mathrm{abs}}\rangle}. \tag{6}$$

The quantity $\zeta(x)$ represents the Riemann ζ-function, and the parameter $\beta = 2$ which is a constant of order unity and depends on the character of the scattering at the boundary (Draine & Lee 1984; Draine 1994). However, the rotational damping time $\tau_{\rm drag,em}$ is insensitive to the exact value of β (Draine & Weingartner 1996). In Eq. (6) it is assumed that emitted photons have an angular momentum $\hbar$ relative to the grain center of mass which is true for $a \ll hc/k_{\rm B}T_{\rm dust} = 800\,(18{\rm K}/T_{\rm dust})\,\mu{\rm m}$ and fulfilled by typical conditions in protoplanetary disks (e.g., Voshchinnikov 2002). The additional damping caused by absorption of photons is smaller than the damping time due to thermal emission by a factor $\sim T_{\rm dust}/T_{\rm rad} \approx 1/500$, where $T_{\rm rad}$ is the color temperature of the dust heating radiation (Purcell 1979), and thus, it is neglected. However, the calculations of this work and of CL 07 show that $(\tau_{\rm drag}/\tau_{\rm drag,gas})^2 \approx 1$ is valid throughout in the disk.

All quantities in Eq. (2) can be extracted from radiative transfer simulations or are fixed parameters, except for the efficiency factor of radiative torques, Q_Γ. The computation of Q_Γ for aspherical dust grains are performed with the DDSCAT software package (Draine & Flatau 1994, 2004; Draine & Weingartner 1996) by Cho & Lazarian (2005) and Lazarian & Hoang (2007) for grains with equivolume radii between 0.1 μm and 100 μm. However, in protoplanetary disks dust grains grow and have sizes of about 1000 μm. For the resulting λ/a ratios, the computational time of DDSCAT increases significantly. For this reason, it is more applicable to approximate Q_Γ (see Fig. 2 in CL 07) with

$$Q_\Gamma = \begin{cases} \sim O(1) & , \text{if } \lambda \sim a, \\ \sim (\lambda/a)^{-1/3} & , \text{if } \lambda > a. \end{cases} \tag{7}$$

Together with Eq. (7), Eq. (2) may be written for $\lambda > a$ as

$$\left(\frac{\omega_{\rm rad}}{\omega_{\rm T}}\right)^2 \approx \left(\frac{\omega_{\rm rad}}{\omega_{\rm T}}\right)^2_{\lambda\sim a} \left(\frac{Q_{\Gamma,\lambda\sim a}}{Q_{\Gamma,\lambda}}\right)^2 \approx \left(\frac{\omega_{\rm rad}}{\omega_{\rm T}}\right)^2_{\lambda\sim a} \left(\frac{\lambda}{a}\right)^{-6}, \tag{8}$$

where

$$\left(\frac{\omega_{\rm rad}}{\omega_{\rm T}}\right)^2_{\lambda\sim a} \approx 4.72 \times 10^9\, \frac{\alpha_1}{\delta^2} \cdot \cdot\, \rho_3 a_{-5} \left(\frac{\gamma_{\rm rad} u_{\rm rad}}{n_{\rm H} k_{\rm B} T}\right)^2 \left(\frac{\lambda}{1\,\mu{\rm m}}\right)^2 \left(\frac{\tau_{\rm drag}}{\tau_{\rm drag,gas}}\right)^2. \tag{9}$$

Grains with rotational energies much higher compared to thermal energy will stably align with the magnetic field. This condition is satisfied by $(\omega_{\rm rad}/\omega_{\rm T})^2 > 10$, as shown in the stability study of Draine & Weingartner (1997). It is assumed that all grains in the current cell are perfectly aligned as soon as $(\omega_{\rm rad}/\omega_{\rm T})^2 > 10$.

3 INTRINSIC THERMAL POLARIZATION

The intrinsic thermal polarization depends on the shape of the dust grains as well as on their relative orientation along the line-of-sight to the observer. The latter is used to trace the magnetic field structure. In this section, we outline the calculation of the instrinsic thermal polarization for individual grains. This provides the basis for the 3D radiative transfer simulations of the net line-of-sight polarization (see Sect. 4)

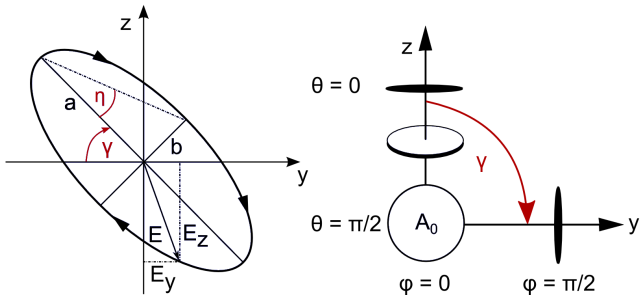

Figure 1. Angle definitions for thermal polarization: *Left:* The polarization ellipse of a light wave **E**. *Right:* The position and orientation of the grain can be defined relative to the observer who is, by definition, observing along the x-axis.

The quantification of polarization of a light wave is given by characteristic intensities, the Stokes parameters, I, Q, U, V (Stokes 1852):

$$\begin{aligned} I &= I, \\ Q &= I_{\rm P} \cos 2\eta \cos 2\gamma, \\ U &= I_{\rm P} \cos 2\eta \sin 2\gamma, \\ V &= I_{\rm P} \sin 2\eta. \end{aligned} \tag{10}$$

where I represents the total (unpolarized) intensity, Q and U characterize the linear polarization, while V represents circular polarization. The factor of two in front of the polarization angle, γ, is due to the fact that any polarization ellipse (see Fig. 1) is indistinguishable from one rotated by 180°. A polarization ellipse is another useful concept to characterize the polarization state of a light wave **E**. It is defined by its direction of rotation, by its inclination relative to a reference axis, the polarization angle, γ, by the relation of its half-axes, η, and its radiant intensity, $c^2 = a^2 + b^2$. The opening angle η can also be expressed in the observer's frame by θ and φ as described in Eq. (16). The factor of two in front of the opening angle of the polarization ellipse, η, in Eq. (10) indicates that an ellipse is indistinguishable from one with the semi-axis lengths swapped accompanied by a 90° rotation.

Aspherical dust grains emit intrinsically polarized waves due to their aspherical shape. The relative orientation of the grain and the observer determines the polarization of the detected wave, characterized by the angles γ, with

$$\gamma = \frac{1}{2} \arctan\left(\frac{U}{Q}\right), \qquad \gamma \in [0, \pi] \tag{11}$$

and η that depends on the orientation of the grain relative to the orientation of the observer. By definition, the observer is observing along the x-axis of a Cartesian system. The polarization angle, γ, and the opening angle of the ellipse, η, can be derived from the angles θ (in the xz-plane) and φ (in the xy-plane) within the observer's frame (see Fig. 1). The projected area of the grain surface is minimized for $\theta = 0$ or $\varphi = \pi/2$, and is maximized for $\theta = \pi/2$ or $\varphi = 0$. For the purposes of this description it is assumed that the grain is of oblate shape with infinitesimal width in one direction as sketched in Fig. 1. However, the behaviour of the relative change in polarization degree is not affected by this

$R_{\rm in}$ [AU]	$R_{\rm out}$ [AU]	Distance [pc]	$a_{\rm dust}$ [μm]	$M_{\rm dust}$ [$M_\odot$]	R_* [$R_\odot$]	T_* [$T_\odot$]
1	200	100	[0.01, 1000]	10^{-6}	2.5	4000

Table 1. Model parameters of the test case *sphere*.

approach. We adjust the simulation to more realistic grain shapes, by adapting the polarization ellipse accordingly to the semi-axes' parameters (a, b) of a given grain shape. In general, the aspherical, irregularly shaped grain must rotate rapidly to be aligned with the magnetic field. Thus, it can be approximated by an ellipsoidal shape. The opening angle η is defined by the projected surface of the grain, $A(\theta, \varphi)$. The minimal projected grain surface, resp. the maximal possible polarization degree is given by the ratio of the grain axes which is a free parameter. Following Fig. (1), $A(\theta, \varphi)$ can be described by

$$A(\theta) = A_0 \left|\sin\theta\right|, \quad A(\varphi) = A_0 \left|\cos\varphi\right|, \tag{12}$$

where A_0 is the maximum of the projected surface. Thus, $A(\theta, \varphi)$ reads

$$A(\theta, \varphi) = A_0 \left|\sin\theta \cdot \cos\varphi\right|. \tag{13}$$

For any symmetric grain, the observed length of its longest grain axis, a, is independent of the observer's position, thus

$$A_0 = \pi a^2. \tag{14}$$

Together with the definition of η,

$$\tan\eta = \frac{b}{a}, \qquad \eta \in \left[-\frac{\pi}{4}, \frac{\pi}{4}\right], \tag{15}$$

where a and b are the half-axes of the polarization ellipse, and the common definition of the area of an ellipse, this results in the opening angle defined by the observer's position:

$$\eta(\theta, \varphi) = \arctan\left|\sin\theta \cdot \cos\varphi\right|. \tag{16}$$

Then, the polarization state of the light wave $\mathbf{E}$ is given by the degree of polarization, P, and the polarization angle, γ (Eq. 11). P can be splitted into a linearly polarized part, $P_{\rm L}$, as well as in a circularly polarized part, $P_{\rm C}$, with

$$P_{\rm L} = \frac{\sqrt{Q^2 + U^2}}{I}, \qquad P_{\rm C} = \frac{V}{I}, \tag{17}$$

Since the magnetic field structure is traced by linear polarization only, we consider only $P_{\rm L}$ to which we refer to as P in the rest of this paper.

4 THE SIMULATION SOFTWARE

This implementation of radiative torques and polarized thermal emission of aspherical dust grains into MC3D has undergone extensive testing. Analytical tests show the high precision of the thermal polarization computations which are accurate down to the numerical limits. However, due to its dependence on the radiation field, the dust grain alignment must be tested numerically, which is presented in Sect. 4.1. Limitations of this approach are discussed in Sect. 4.2.

4.1 Test case: Spherical density distribution

To test the implementation of the dust grain alignment we choose a spherical dust density distribution, $\rho(r) \sim r^{-1}$, with further model parameters described in Tab. 1. For this model, distributions of temperature, anisotropy of the radiation field, and dust grain alignment have been computed self-consistently (see Fig. 2). The numerical grid of this 1-dimensional test problem is discretized in $N_{\rm r} = 256$ cells on which the distributions of temperature, the degree of anisotropy of the radiation field, and grain alignment efficiency are computed at 45 discrete logarithmically distributed wavelengths within $[1\,\mu{\rm m}, 1000\,\mu{\rm m}]$ with 10^7 photons.

The temperature distribution, $T(r)$, of a spherical density distribution heated only by a central star shows the expected radial decrease. Close to the central star where dust density and stellar radiation are have reached their maximum values, the temperature reaches its maximum, as well. Towards the boundaries of the model space, it is decreasing radially.

The anisotropy of the radiation field, $\gamma_{\rm rad}(r)$, is slightly increasing radially. Being located close to the central star its isotropic reemission of high-energy photons results in an anisotropy of the net radiation field. At radii with decreasing temperatures, the dust emits less high-energy photons, while photons from the central regions are efficiently shielded by absorption of the more dense inner regions. In the boundary cells, the anisotropy of the radiation field reaches its maximum. Due to the negligence of an external radiation field, photons are only able to enter these cells from more inner regions.

The alignment efficiency of dust grains, $(\omega_{rad}/\omega_T)^2$, is very sensitive to the ratio of temperature, energy density of the radiation field, and degree of anisotropy of the radiation field, as well as to the local mass density (see Eq. 8). In general, $(\omega_{rad}/\omega_T)^2$ exceeds 10 throughout the entire model space, resulting in an alignment of all grains in this test case. As expected for the given model, the value of $(\omega_{rad}/\omega_T)^2$ decreases radially with temperature, energy density, and mass density.

4.2 Limitations of this implementation

Although the polarization of dust emission of aligned dust grains has been implemented successfully, there are limitations to this approach that are discussed here:

i) Grain alignment: In the description of grain alignment we assume that all grains within a given cell are aligned perfectly as soon as $(\omega_{\rm rad}/\omega_{\rm T})^2 > 10$ (Draine & Weingartner 1996, 1997).

ii) Scattering: For the implementation of aspherical dust grains into MC3D, we apply a hybrid approach regarding the dust grain shape. During the self-consistent calculations of temperature distribution and anisotropy of the radiation field, scattering effects under consideration of both a dust grain size distribution and a broad wavelength spectrum are indispensable. Scattering by spherical grain shapes is relatively easy to handle numerically (e.g., Mie scattering). However, scattering by aspherical grain shapes over a broad range of grain sizes and wavelengths is still an issue for the mathematical description and numerical implementa-

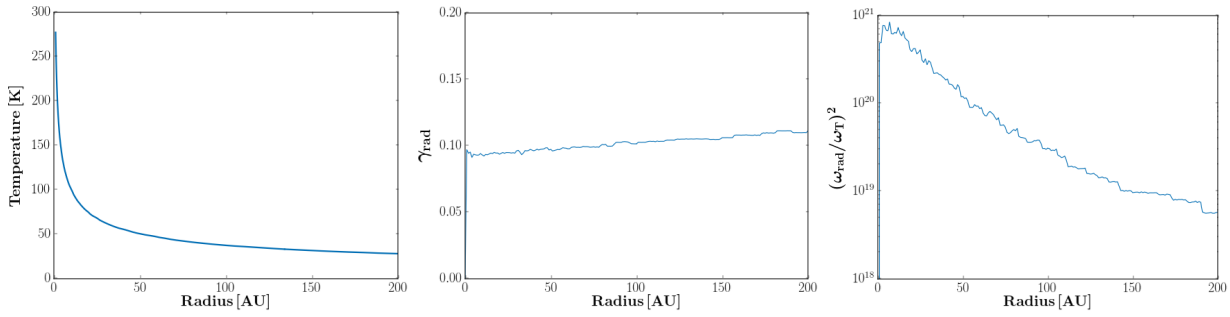

Figure 2. A SPHERICAL DUST DENSITY DISTRIBUTION in temperature T (*left*), degree of anisotropy of the radiation field γ_{rad} (*center*), and dust grain alignment efficiency $(\omega_{rad}/\omega_T)^2$ (*right*).

tion (Voshchinnikov 2004). For that reason, MC3D processes the photons through the model space assuming spherical grain shapes during the computation of dust temperature distributions and anisotropy of the radiation field, and skips to aspherical grains for calculating the polarization state. Here, the scattering is neglected, and thus, the significance of these simulations is limited to long wavelengths where scattering effects play only a tangential role for observations of protoplanetary disks. However, this study already opens unprecedented possibilities to investigate the effects of polarized dust emission and grain alignment in protoplanetary disks.

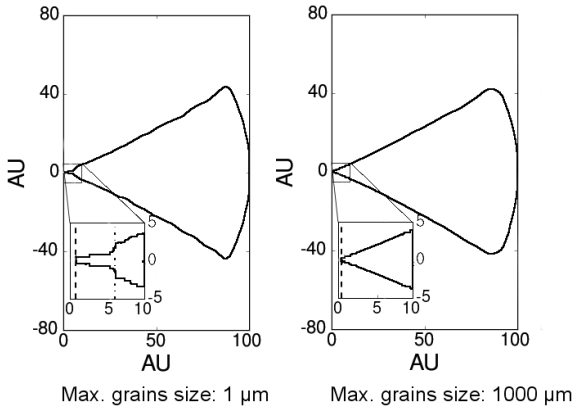

Figure 3. GRAIN ALIGNMENT IN THE DISK (shown perpendicularly to the disk mid-plane) with maximum grain sizes of 1 μm *(left)* and 1000 μm *(right)*. Within the black contour lines, the grain alignment efficiency exceeds the threshold of 10, i.e., the grains are aligned. Small grains start to align close to the mid-plane at $r \geq 0.7$ AU (*dashed line*), at $r \geq 6$ AU (*dashed-dotted line*) grains also align towards the disk surface. Large grains with radii $\leq 1000\,\mu$m have only one initiation of grain alignment at $r = 0.08$ AU. These findings correspond very well to the findings of CL 07 (Fig. 3, Fig. 4; $r \gtrsim 0.7$ AU in the surface layer and $r \gtrsim 0.05$ AU in the disk interior).

5 APPLICATIONS

This 3D radiative transfer study, now including polarized dust emission of aspherical grains, aims at modeling, characterizing, and explaining polarimetric observations of T-Tauri disks. Applications of these new features are discussed here with the goal of comparing the results of this study with the findings described in the study of CL 07. Note that, due to the partly significant differences of both approaches (the work of CL 07 assumes, e.g., isothermality of the disk interior, limitations of possible photon paths, and neglection of the orientation of polarization vectors in SED simulations) the evaluation can only be done qualitatively. Yet, due to the lack of other work on thermal polarization simulations of aligned dust grains in protoplanetary disks, this method is the most suitable.

In both studies, the magnetic field is assumed to be regular and toroidal, and both assume a flared disk structure. This study uses the approach of Shakura & Sunyaev (1973),

$$\rho(R,\,z) = \rho_0 \left(\frac{R}{r_0}\right)^{-\alpha} \exp\left(-\frac{1}{2}\left[\frac{z}{h(R)}\right]^2\right),\; h(R) = h_0 \left(\frac{R}{r_0}\right)^{\beta} \quad (18)$$

with $\alpha = 1.2$, $\beta = 1.14$ and with the same power-law for the grain size distribution as applied by CL 07, $dN \propto a^{-3.5}\mathrm{d}a$ (Mathis et al. 1977). We assume a grain composition of a mix of 62.5% astronomical silicate and 37.5% graphite with a total bulk density of $2.7\,g\,cm^{-3}$ and a continual grain size distribution (Tab. 2; Weingartner & Draine 2001), while CL 07 consider only astronomical silicate, with and without water ice mantle, arranged in a thin surface layer ($a_{max} = 1\,\mu$m) and the disk interior ($a_{max} = 1000\,\mu$m). Furthermore, this study computes the temperature distribution of the disk and the anisotropy of the radiation field self-consistently based on the Monte-Carlo radiative transfer method and assumes local thermodynamic equilibrium in each grid cell only. CL 07 limit the radiation flux from the surface layer and the disk interior to a narrow spectrum around the wavelength $\sim 3000/T_{ds,i}\,\mu$m, limit the direction of the radiation flow within the disk to the vertical direction only, and assume that the disk interior is isothermal. Both models neglect effects of polarizing scattering. Indeed, effects of scattering are less important in the submillimeter/millimeter wavelength regime.

In order to compare both implementations to each other, we choose a parameter setup similar to the setup of parameters of CL 07 (see Tab. 2). In the following, the grain alignment in the disk as well as the resulting SEDs and polarization maps are discussed.

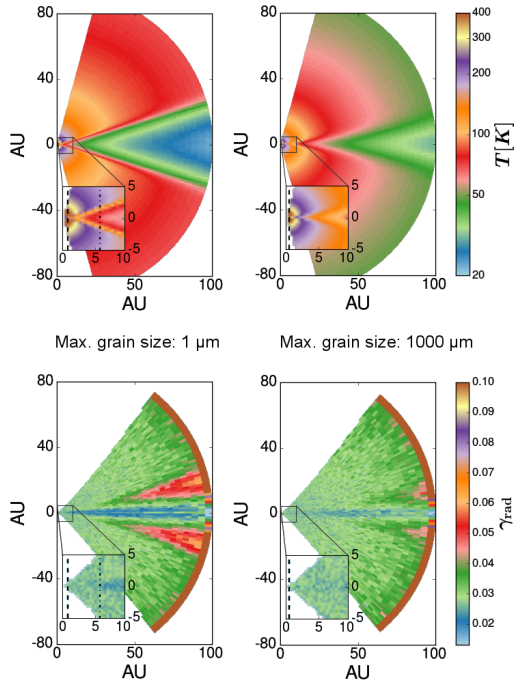

Figure 4. Temperature distribution and anisotropy of the radiation field in the disk. *Top:* The temperature distribution of the disk perpendicular to its mid-plane for $a_{\max} = 1\,\mu$m (*top left*) and $a_{\max} = 1000\,\mu$m (*top right*). *Bottom:* The anisotropy of the radiation field in the case of $a_{\max} = 1\,\mu$m (*bottom left*) and $a_{\max} = 1000\,\mu$m (*bottom right*). The different maximal grain sizes change the optical depth of the disk. The optical thick disk (*left*) shows sharp gradients in anisotropy and temperature, the optical thin(er) disk (*right*) shows much smoother gradients. While the smoother gradients lead to only one onset of grain alignment (dashed lines), the sharp gradients benefit the second jump in grain alignment (dashed-dotted line).

Table 2. Initial parameters for the case *protoplanetary disk*.

$R_{\rm in}$ [AU]	$R_{\rm out}$ [AU]	Distance [pc]	$a_{\rm dust}$ [μm]	$M_{\rm dust}$ [$M_\odot$]	R_* [$R_\odot$]	T_* [$T_\odot$]
0.02	100	140	[0.01, 1000]	10^{-4}	2.5	4000

5.1 Grain alignment in disks

The dust grain alignment perpendicular to the mid-plane of the protoplanetary disk is shown in Fig. 3. For this study, two simulations with corresponding maximal grain sizes are presented since CL 07 discuss the surface layer ($a_{\max} = 1\,\mu$m) and the disk interior ($a_{\max} = 1000\,\mu$m) separately. We apply a grid with logarithmic spacing to spatially resolve the inner region of the disk on a level of 10^{-3} AU (for more details on the grid architecture, see Wolf et al. 1999; Wolf 2003). This study demonstrates that the alignment of grains is dependent on the grain size. Small grains with radii $\leq 1\,\mu$m show two initialization steps of grain alignment, the first step in the mid-plane of the disk at $r \approx 0.7$ AU, the second step towards the surface of the disk at $r = 6$ AU. The first step corresponds very well to the starting point of grain alignment in the study of CL 07. The grain alignment depends significantly on the ratio of temperature, energy density, and anisotropy of the radiation field, as well as on the local mass density (see Eq. 8). Small grains are very poor absorbers and emitters of radiation, thus, the disk with $a_{\max} \leq 1\,\mu$m is optically thick. As a result, temperature and anisotropy of the radiation field rapidly decrease with distance to the center of the disk. At the initial point of the dust grain alignment towards the surface of the disk, at $r = 6$ AU, sharp gradients are present in the anisotropy of the radiation field and in the temperature distribution (see Fig. 4) resulting in $(\omega_{\rm rad}/\omega_{\rm T})^2$ which then exceeds 10 slightly.

Large grains with radii $\leq 1000\,\mu$m have one initiation of grain alignment at $r = 0.08$ AU what again corresponds very well to the findings of CL 07 who determined the initialization point for large grains in their disk interior to $r = 0.05$ AU (see Fig. 3). Large grains are much more efficient in re-emitting the absorbed radiation. As a result, they cool down more efficiently, are optically thin(er) compared to small grains, and have much smoother gradients in temperature and anisotropy of the radiation field.

5.2 Spectral energy distribution

The spectral energy distributions for polarized dust emission of aligned aspherical grains computed within the context of this study are shown in Fig. 5 and compared to the SEDs in CL 07, Fig. 8. The SEDs of both models show an emission peak around 10 μm which is the characteristic peak of silicate (Draine & Lee 1984). Additionally to this, the SED of CL 07 shows a second and third peak at 40 μm and 60 μm caused by the water ice mantle of the grains in their model. CL 07 ignored the orientation of polarization vectors in their calculations of the SEDs. The observed polarization degree is very sensitive to the orientation of polarization vectors, especially in the case of aligned dust grains. The new features of the study presented in this work consider this effect. With a disk inclination of $i = 10°$, a good agreement with the calculations of CL 07 was found by comparison of the behavior of the total emission relative to the polarized emission in both studies. As expected from the optical properties with respect to the wavelength, large dust grains dominate the emission spectrum at long wavelengths. This is seen in the total emission and the polarized emission in both studies. CL 07 and this work are neglecting polarizing scattering effects. With respect to the model differences, the relative behavior of total to polarized emission of both grain size distributions of CL 07 and this work fit well to each other.

Furthermore, we find polarization degrees, P, for both models in the order of $\sim$ 10% across long wavelengths (Fig. 5). At wavelengths below 100 μm, the strength of the intrinsically polarized emission drops significantly.

5.2.1 *The effect of inclination on spectro-polarimetry*

Since polarimetry is very sensitive to projection effects as well as to spatial resolution, the inclination of the disk is a mayor influence on the detected polarized signal. Because of the radial symmetry of the polarization pattern stemming from a toroidal magnetic field structure if the disk is face-on oriented to the observer, the polarized signal will be extinguished. Thus, the disk inclination can be derived from spectro-polarimetric observation, also in cases where this is not possible in unpolarized light.

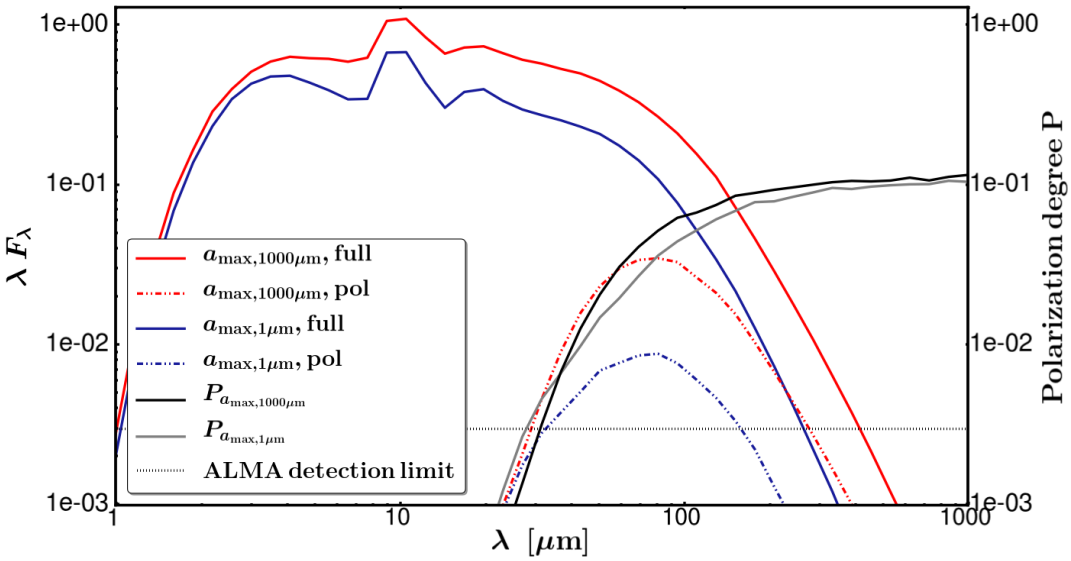

Figure 5. Spectral Energy Distribution. The vertical axes (λF_λ and P) are in arbitrary units. Total (full) emission of the model with $a_{\rm max} = 1\,\mu$m (blue solid line), polarized emission for $a_{\rm max} = 1\,\mu$m (blue dashed-dotted line), and total emission of the model with $a_{\rm max} = 1000\,\mu$m (red solid line), polarized emission for $a_{\rm max} = 1000\,\mu$m (red dashed-dotted line); all models are computed at a disk inclination of $i = 10°$. The polarization degree of both models is given by the black/grey line. The detection limit for polarization of extended sources with ALMA is given by the black dotted line. Our findings correspond to the findings shown in CL 07, Fig. 8, qualitatively. Note that CL 07 ignored the direction of polarization vectors for these calculations.

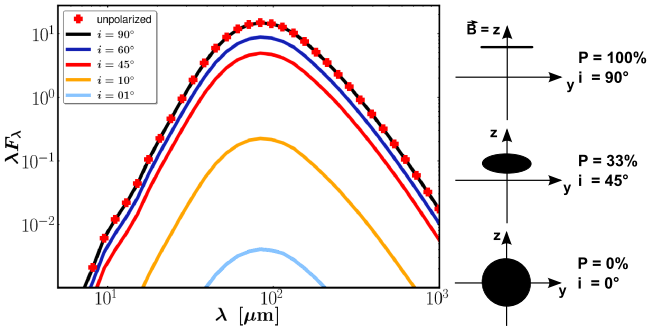

Figure 6. Spectro-polarimetry of a sphere containing a homogenous magnetic field. The effect of inclination is clearly identifiable in the SED of the polarized emission. At an inclination $i = 90°$ the observer looks directly at the edge of all dust grains, thus the emission increases to its maximum ($P = 100\%$, assuming razor-thin dust grains). By changing inclination towards a face-on observation of the dust grains, the polarization degree drops to $P = 33\%$ at $i = 45°$ and becomes $P = 0\%$ at the face-on position where $i = 0°$.

In this section, the effect of polarization on SEDs is shown for an illustrating toy model as well as for a model of a protoplanetary disk.

The illustrating toy model: A sphere

The most simple case for spectro-polarimetry is a spherical dust distribution, $\rho_{\rm dust}(r)$, containing a homogenous magnetic field $\mathbf{B}$,

$$\rho_{\rm dust}(r) \sim r^{-1}, \qquad \mathbf{B} \sim \mathbf{e}_{\rm z}, \tag{19}$$

where $\mathbf{e}_{\rm z}$ is the unit vector in z-direction. To restrict the analysis only to effects of inclination, all dust grains are assumed to be perfectly aligned to the magnetic field. The total (unpolarized) emission of this spherical symmetric model is independent of the inclination (Fig. 6). However, by changing the inclination from an edge-on position to a face-on position relative to the aspherical dust grain, the polarization degree changes. The polarization degree is maximal ($P = 100\%$ in the case of a razor-thin grain) at the edge-on position ($i = 90°$), drops to $P = 33\%$ at an inclination of $i = 45°$, and at the face-on position ($i = 0°$) the polarization degree disappears ($P = 0\%$; Fig. 6). Thus, by determining the SED of the polarized dust emission relative to the unpolarized radiation, the inclination of the object can be derived from the SED. A model of a protoplanetary disk is discussed in the next section.

The protoplanetary disk

SEDs of the polarized emission of aspherical dust grains in a protoplanetary disk have been computed based on dust grain alignment simulations. In Fig. 7, the SEDs are shown for the case of large grains with $a_{\rm max} = 1000\,\mu$m. The characteristic $10\,\mu$m silicate feature is clearly seen in all SEDs. The disk is optically thin, thus its SEDs at different inclination angles are indifferent in total emission. It is prominent that the SEDs in polarized light are indistinguishable for high inclinations ($i \gtrsim 45°$). In these cases, the polarization pattern observed at high inclinations is dominated by parallel polarization vectors (Fig. 8). A significant drop in the amplitude of the SEDs is found for lower inclinations ($i < 45°$). As it is expected from the radial symmetric polarization pattern corresponding to a toroidal magnetic field structure, the signal tends to vanish with very small inclinations.

As shown here, the inclination of the disk affect the SED in polarized light additionally to the common physical parameters derived from SEDs, such as chemical dust composition or dust grain size. These simulations show that it is possible to distinguish between different models of proto-

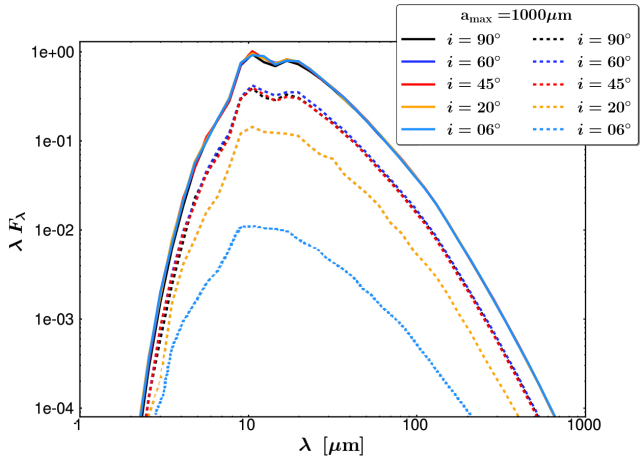

Figure 7. SPECTRO-POLARIMETRY OF A PROTOPLANETARY DISK containing a toroidal magnetic field, computed for a maximal dust grain size of 1000 μm. The total (unpolarized) emission is shown in *solid lines*, the polarized emission in *dashed lines* both at different inclinations i, the intensity (λF_λ) is in arbitrary units. Note that the solid lines are overlapping each other.

planetary disks and magnetic fields therein by taking into account not only the SED in the unpolarized light but also the polarization information that is carried by the radiation.

5.3 Spatially resolved polarization maps.

Previous observations performed with SMA and CARMA traced the polarization information sparsely with low spatial resolution (e.g., Stephens et al. 2014) or resulted in non-detections (Hughes et al. 2009, 2011). Due to the clear discrepancy between those observations and theoretical models (e.g., CL 07; Bertrang et al. 2017, and this work), it was suggested to perform more sensitive observations of the dust polarization (Stephens et al. 2014). With the Atacama Large (Sub)Millimeter Array (ALMA) it is now possible to spatially resolve protoplanetary disks and measure their polarized dust emission on a highly resolved level for the first time (Kataoka et al. 2016).

Thus, spatially resolved radiative transfer simulations of the polarized dust emission are necessary to analyze such observations.

Figure 8 shows simulations of spatially resolved observations of intrinsically polarized radiation of a protoplanetary disk compared to the maps shown in CL 07. The underlying magnetic field structure is toroidal and the dust grain alignment is computed as described in Eq. (8). All maps show simulated observations at a wavelength of 850 μm at two different disk inclinations of 10° and 60°. The maps display the characteristic polarization pattern of an underlying toroidal magnetic field structure. At a nearly face-on inclination of i = 10°, the radially symmetric pattern is clearly visible in the results of both codes and the polarization degree is nearly constant as expected. Only four vectors in the maps of CL 07 show an increase in polarization degree what is potentially caused by boundary effects. The polarization angle, the vector orientation (Figure 8, left column), indicates a homogenous field structure but the polarization degree (Figure 8, center column) implies a twist in the orientation of aligned dust grains caused by the toroidal field structure. However, without the knowledge of the underlying magnetic field structure, the drop in the polarization degree may be as well interpreted as a lack of order in the magnetic field, and thus, an insufficiently strong magnetic field influence in this region.

In the more inclined maps (i = 60°), the radial polarization pattern converts into a rather hourglass-shaped structure which results from the projection effect along the line-of-sight and is found in both maps. The same also applies to the degree of polarization. Close to the vertical symmetry axis, the polarization signal is the strongest and drops only slowly towards the center of the disk. Along the horizontal symmetry axis of the disk, the polarization signal is canceled out almost completely due to projection effects. Only with increasing distance to this axis, the polarization signal becomes stronger again. This behaviour is found in both studies. The polarization pattern shows the characteristic radial polarization structure of a purely toroidal magnetic field as well as the drop of the polarization degree towards the center of the disk. The observations of face-on oriented disks are the ideal case for identifying this radially symmetric magnetic field structure. It is obvious that spatially unresolved observations of such structures would lead to a non-detection because of the radial symmetry of the polarization pattern. In unresolved face-on observations of a protoplanetary disk, the polarization states of the waves emitted from different points in that disk will cancel each other out. Therefore, the spatial resolution is essential for polarization observations of protoplanetary disks performed with the polarization modes of, e.g., ALMA. These new simulations of the polarized thermal dust emission can be directly compared to future ALMA observations by applying the *Common Astronomy Software Applications package* (CASA *v* 4.5.2; Fig. 9). In the more inclined map (i = 60°), we find the same behaviour of the polarization vectors in the simulated ALMA observations as in the pure radiative transfer simulations. However, in the rather face-on map (i = 10°), we find a polarization nulling in the center of the disk caused by blurring of Stokes Q and U in the simulated observation.

The tool presented in this study can be used to derive physical parameters from observations of polarized dust emission, or to predict observational results, by adaption of the parameters of the underlying disk, dust, and magnetic field model.

It is interesting to compare the instrinsic thermal polarization to the effect of self-scattering. In recently published calculations on the effect of self-scattered thermal emission spherical dust grains were assumed (Kataoka et al. 2015, 2016; Yang et al. 2016). These models show an upper limit to the polarization degree of $\sim$ 3%. Moreover, they show that the expected polarization structure created by self-scattering has circular symmetry, while deviations can occur with changing optical depth. As pointed out in this work, the polarization degree resulting from the intrinsical thermal polarization depends not only on the relativ orientation of grains along the line-of-sight. Instead, the maximal polarization degree also depends on the axis ratio of the grains. The grain axis ratio, on the other hand, is a free parameter. Thus, the intrinsic polarization does not show a strong upper limit in the degree of polarization such as self-scattering.

Polarization degrees of ~ 10%, which exceed the upper limit of self-scattering polarization, as observed in the protoplanetary disk HD142527 (Kataoka et al. 2016) can be explained by the instrinsic thermal polarization of dust grains with axis ratios of 1:1.3 (see Figs. 8, 9).

6 CONCLUSIONS

The 3D radiative transfer study that has been presented in this work considers dust grain alignment and polarized dust emission of aspherical grains. This tool enables the comprehensive analysis of (sub-)mm observations of polarized radiation of protoplanetary disks performed with, e.g., ALMA. The major features, implemented in the context of this work, are the following.

(i) This study makes use of a hybrid approach to solve the scattering problem (i.e., scattering by aspherical grains) that combines treatment of spherical and aspherical grain shape models.
(ii) The anisotropy of the radiation field, as well as the efficiency of dust grain alignment is computed for a given dust and disk model.
(iii) We find that the alignment efficiency exceeds the threshold of 10 throughout our models of typical protoplanetary disks. This implies that grain alignment in disks is expected to be a rather common phenomenon. However, a broader parameter study is needed in order to strengthen this finding.
(iv) SEDs of the polarized emission of aligned aspherical dust grains are a tool to distinguish between different disk models and magnetic fields therein, where SEDs of the total (unpolarized) emission are indistinguishable.
(v) Spatially resolved polarization maps trace the intrinsically polarized dust emission of protoplanetary disks depending on dust and disk parameters. These simulated polarization maps enable the preparation and analysis of observations of polarized dust emission performed with, e.g., ALMA.

The unprecedented sensitivity and resolution of ALMA finally allow for spatially observations of the polarized dust emission of protoplanetary disks. The polarization signal which was previously canceled out by a lack of sufficient spatial resolution, is now observable. Such observations need to be analysed by radiative transfer simulations as those presented in this work. In this way, differences in underlying dust, disk, and magnetic field models can be revealed. Most recently, (Tazaki et al. 2017) emphasized that magnetic fields might be preferentially detectable through mid-infrared polarimetric observations. The applicability of our analysis tools to this wavelength range will be considered in a future study. Studies such as the presented work are essential to finally observationally constrain the magnetic field influence on the evolution of protoplanetary disks.

ACKNOWLEDGEMENTS

GHMB gratefully acknowledges financial support by the DFG under contract WO857/11-1 within the frame of the DFG Priority Program1573: The Physics of the Interstellar Medium, as well as by the Millennium Science Initiative (Chilean Ministry of Economy), through grant Nucleus RC13007.

REFERENCES

Andersson B.-G., Lazarian A., Vaillancourt J. E., 2015, ARA&A, 53, 501
Balbus S. A., Hawley J. F., 1991, ApJ, 376, 214
Balbus S. A., Hawley J. F., 1998, RMP, 70, 1
Balbus S. A., Hawley J. F., Stone J. M., 1996, ApJ, 467, 76
Bertrang G. H.-M., Flock M., Wolf S., 2017, MNRAS, 464, L61
Bethell T. J., Chepurnov A., Lazarian A., Kim J., 2007, ApJ, 663, 1055
Chiang E. I., Joung M. K., Creech-Eakman M. J., Qi C., Kessler J. E., Blake G. A., van Dishoeck E. F., 2001, ApJ, 547, 1077
Cho J., Lazarian A., 2005, ApJ, 631, 361
Cho J., Lazarian A., 2007, ApJ, 669, 1085
Ciesla F. J., 2007, ApJ, 654, L159
Cleeves L. I., Bergin E. A., Qi C., Adams F. C., Öberg K. I., 2015, ApJ, 799, 204
Davis Jr. L., Greenstein J. L., 1951, ApJ, 114, 206
Dolginov A. Z., Mytrophanov I. G., 1976, Ap&SS, 43, 291
Draine B. T., 1994, in Cutri R. M., Latter W. B., eds, Astronomical Society of the Pacific Conference Series Vol. 58, The First Symposium on the Infrared Cirrus and Diffuse Interstellar Clouds. p. 227
Draine B. T., Flatau P. J., 1994, Journal of the Optical Society of America A, 11, 1491
Draine B. T., Flatau P. J., 2004, ArXiv Astrophysics e-prints,
Draine B. T., Lee H. M., 1984, ApJ, 285, 89
Draine B. T., Weingartner J. C., 1996, ApJ, 470, 551
Draine B. T., Weingartner J. C., 1997, ApJ, 480, 633
Dzyurkevich N., Flock M., Turner N. J., Klahr H., Henning T., 2010, A&A, 515, A70
Flock M., Dzyurkevich N., Klahr H., Turner N. J., Henning T., 2011, ApJ, 735, 122
Flock M., Ruge J. P., Dzyurkevich N., Henning T., Klahr H., Wolf S., 2015, A&A, 574, A68
Hughes A. M., Wilner D. J., Cho J., Marrone D. P., Lazarian A., Andrews S. M., Rao R., 2009, ApJ, 704, 1204
Hughes A. M., Wilner D. J., Andrews S. M., Qi C., Hogerheijde M. R., 2011, ApJ, 727, 85
Hughes A. M., Hull C. L. H., Wilner D. J., Plambeck R. L., 2013, AJ, 145, 115
Kataoka A., et al., 2015, ApJ, 809, 78
Kataoka A., et al., 2016, preprint, (arXiv:1610.06318)
Lazarian A., 2007, J. Quant. Spectrosc. Radiative Transfer, 106, 225
Lazarian A., Hoang T., 2007, ApJ, 669, L77
Lazarian A., Andersson B. G., Hoang T., 2015, in Kolokolova L., Hough J., Levasseur-Regourd A.-C., eds, , Polarimetry of Stars and Planetary Systems. Cambridge University Press
Lynden-Bell D., Pringle J. E., 1974, MNRAS, 168, 603
Mathis J. S., Rumpl W., Nordsieck K. H., 1977, ApJ, 217, 425
Purcell E. M., 1969, Physica, 41, 100
Purcell E. M., 1979, The Astrophysical Journal, 231, 404
Purcell E. M., Spitzer Jr. L., 1971, ApJ, 167, 31
Rao R., Girart J. M., Lai S.-P., Marrone D. P., 2014, ApJ, 780, L6
Roberge W. G., Degraff T. A., Flaherty J. E., 1993, ApJ, 418, 287
Segura-Cox D. M., Looney L. W., Stephens I. W., Fernández-López M., Kwon W., Tobin J. J., Li Z.-Y., Crutcher R., 2015, ApJ, 798, L2

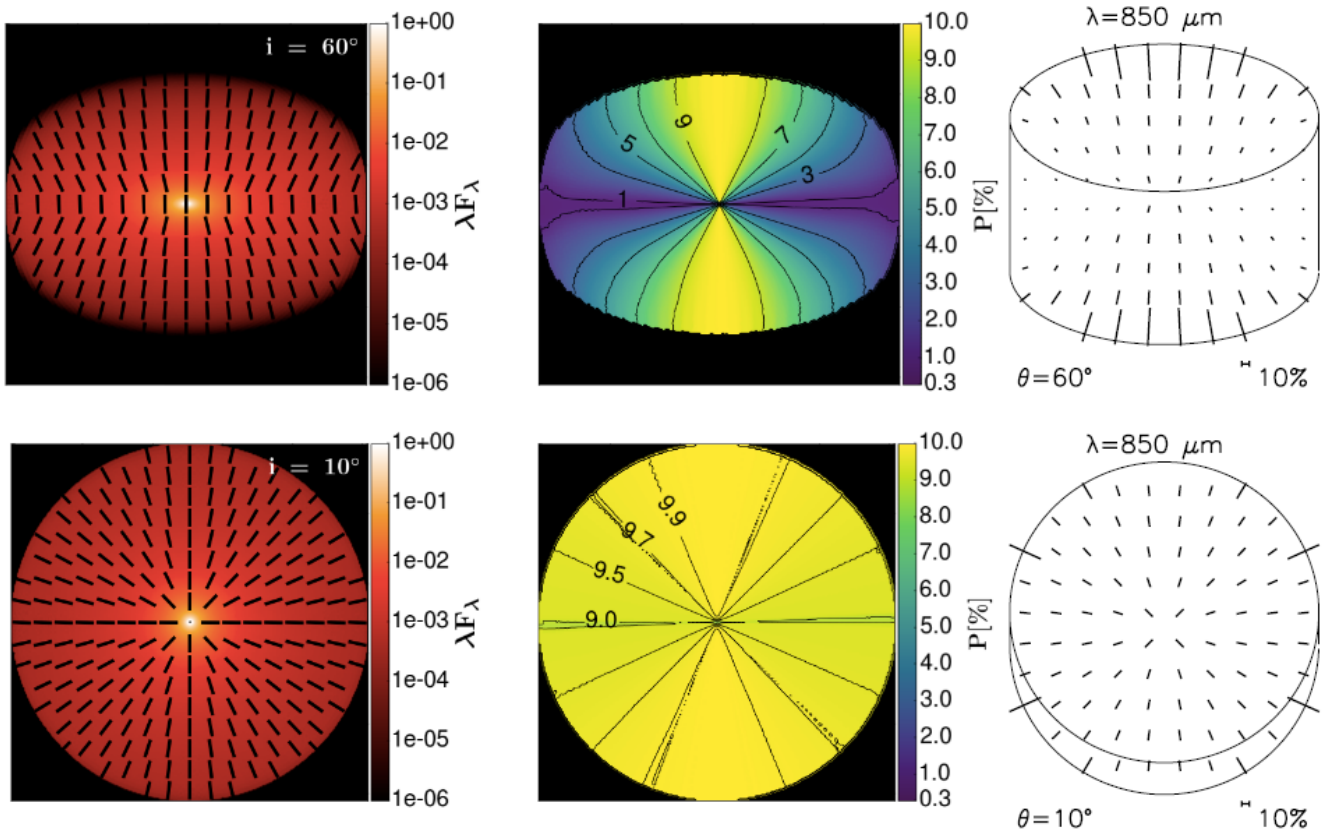

Figure 8. Polarization maps, *left:* this work, showing total intensities in arbitrary units over-plotted by polarization vectors of unit length at a wavelength of 850 μm and disk inclinations of $i = 60°$ ($a_{\rm max} = 1000\,\mu$m, *top left*) and $i = 10°$ (*bottom left*). *Center:* Corresponding maps of the polarization degree, $\boldsymbol{P}$, over-plotted by contour lines of $\boldsymbol{P}$. Values of $\boldsymbol{P}$ below the detection limit of ALMA ($\boldsymbol{P} = 0.3\%$) are marked in black. *Right:* Thermal polarization maps from CL 07 (reproduced with permission by AAS) at a wavelength of 850 μm of the emission of disk interior + surface layer at two disk inclinations $\theta = 60°$ (*top left*) and $\theta = 10°$ (*bottom left*).

Semenov D., Wiebe D., 2011, ApJS, 196, 25
Shakura N. I., Sunyaev R. A., 1973, A&A, 24, 337
Stephens I. W., et al., 2014, Nature, 514, 597
Stokes G. G., 1852, Transactions of the Cambridge Philosophical Society, 9, 399
Tazaki R., Lazarian A., Nomura H., 2017, preprint, (arXiv:1701.02063)
Turner N. J., Sano T., Dziourkevitch N., 2007, ApJ, 659, 729
Turner N. J., Fromang S., Gammie C., Klahr H., Lesur G., Wardle M., Bai X.-N., 2014, PP VI, pp 411–432
Voshchinnikov N. V., 2002, in Videen G., Kocifaj M., eds, Optics of Cosmic Dust. p. 1 (arXiv:astro-ph/0303162)
Voshchinnikov N. V., 2004, Astrophysics and Space Physics Reviews, 12, 1
Weingartner J. C., Draine B. T., 2001, ApJ, 548, 296
Weintraub D. A., Goodman A. A., Akeson R. L., 2000, PP IV, p. 247
Wolf S., 2003, CPC, 150, 99
Wolf S., Henning T., Stecklum B., 1999, A&A, 349, 839
Yang H., Li Z.-Y., Looney L., Stephens I., 2016, MNRAS, 456, 2794

This paper has been typeset from a TEX/LATEX file prepared by the author.

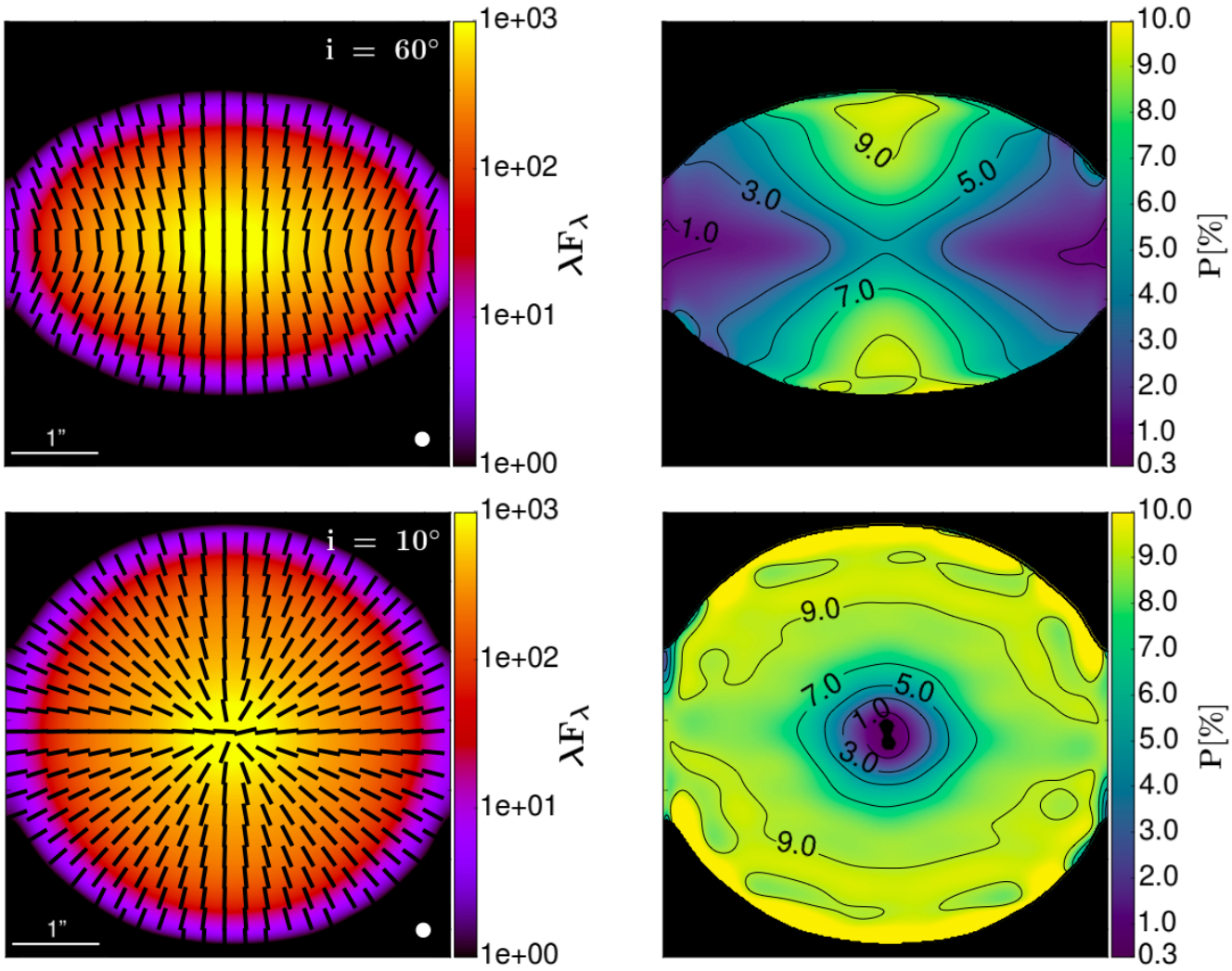

Figure 9. Simulated ALMA observations (CASA v4.5.2, band 6, configuration C40-5, spatial resolution of 0.23", including thermal noise) of the intrinsically polarized dust emission at an two different inclinations i. *Left:* Total intensity map in arbitrary units over-plotted by polarization vectors of unit length indicating the polarization angle only. The polarization vectors are binned over one beam (indicated by the white ellipse). *Right:* Corresponding maps of the polarization degree, P, over-plotted by contour lines of P. Values of P below the detection limit of ALMA (P = 0.3%) are marked in black. Note that,in the case of a (almost) face-on disk, the observed Stokes parameters Q and U blur in the center of the disk, resulting in a nulling of the polarized signal.